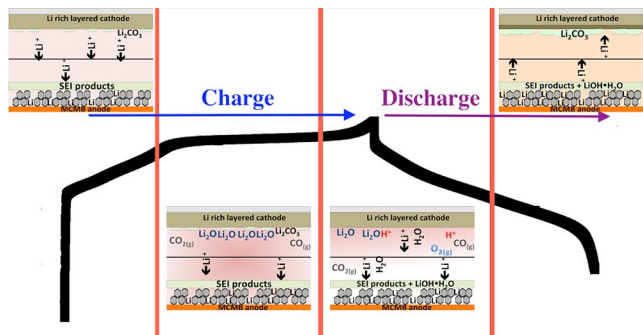


The following graphic will be used for the TOC:



1 Direct *In situ* Observation of Li_2O Evolution on Li-Rich High-Capacity 2 Cathode Material, $\text{Li}[\text{Ni}_x\text{Li}_{(1-2x)/3}\text{Mn}_{(2-x)/3}]\text{O}_2$ ($0 \leq x \leq 0.5$)

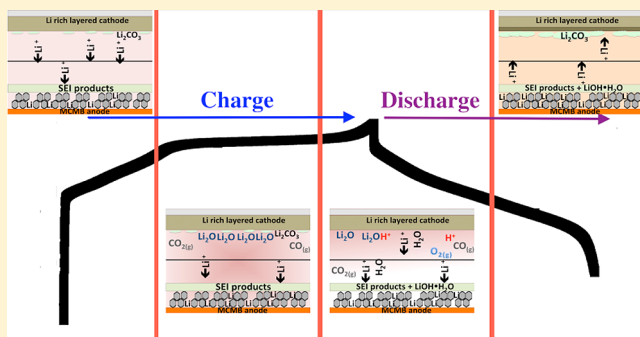
3 Sunny Hy,[†] Felix Felix,[†] John Rick,[†] Wei-Nien Su,[†] and Bing Joe Hwang*,^{†,‡}

4 [†]Nanoelectrochemistry laboratory, Department of Chemical Engineering, National Taiwan University of Science and Technology,
5 Taipei, Taiwan 10607

6 [‡]National Synchrotron Radiation Research Center, Hsin-Chu, Taiwan 30076

7 Supporting Information

8 **ABSTRACT:** High-capacity layered, lithium-rich oxide cathodes show great promise for use as positive electrode materials
9 for rechargeable lithium ion batteries. Understanding the
10 effects of oxygen activating reactions on the cathode's surface
11 during electrochemical cycling can lead to improvements in
12 stability and performance. We used *in situ* surface-enhanced
13 Raman spectroscopy (SERS) to observe the oxygen-related
14 surface reactions that occur during electrochemical cycling on
15 lithium-rich cathodes. Here, we demonstrate the direct
16 observation of Li_2O formation during the extended plateau
17 and discuss the consequences of its formation on the cathode
18 and anode. The formation of Li_2O on the cathode leads to the
19 formation of species related to the generation of H_2O together
20 with LiOH and to changes within the electrolyte, which eventually
21 result in diminished performance. Protection from, or
22 mitigation of, such devastating surface reactions on both electrodes
23 will be necessary to help realize the potential of high-capacity
cathode materials (270 mAh⁻¹ versus 140 mAh⁻¹ for LiCoO_2) for practical applications.



24 ■ INTRODUCTION

25 Lithium-rich cathode materials, represented in solid solution
26 notation as $\text{Li}[\text{Ni}_x\text{Li}_{(1-2x)/3}\text{Mn}_{(2-x)/3}]\text{O}_2$ ($0 \leq x \leq 0.5$)¹ or in
27 composite notation as $x\text{Li}_2\text{MnO}_3 \cdot (1-x)\text{LiMn}_{0.5}\text{Ni}_{0.5}\text{O}_2$ ^{2,3}
28 (LLNMO), have generated a large amount of interest over
29 the past decade due to their high reversible capacities (>270
30 mAh/g).^{4–8} Ohzuku et al.⁹ demonstrated that the capacity can
31 reach 300 or even 350 mAh/g using slower rates or higher
32 temperatures, respectively.⁹ However, the charging mechanism
33 is still uncertain,^{7,10} while additionally the surface structural
34 changes that lead to capacity fade and instability remain
35 unresolved. Ito et al.¹¹ showed that there is continuous
36 formation of Li_2CO_3 on the cathode's surface with subsequent
37 decomposition as the result of oxygen reduction during
38 discharge below 3.0 V. Similarly, Hong et al.¹² performed *ex*
39 *situ* FTIR and showed Li_2CO_3 formation and subsequent
40 decomposition upon discharging and charging, which they
41 described as being attributable to the involvement of oxygen
42 radicals. Lu et al.⁸ first proposed the extraction of Li_2O from
43 LLNMO, during the plateau region with the simultaneous
44 extraction of Li and O, to explain its anomalously high capacity.
45 However, Li_2O has not been directly observed in this region
46 and has only been tentatively observed in the discharged state
47 by *ex situ* time-of-flight secondary ion mass spectroscopy, where
48 Li_2O^+ and Li_2C_2^+ were observed and may be generated from not
49 only Li_2O but also from LiO_2 , Li_2O_2 , Li_2CO_3 , etc.¹¹ Due to the
50 sensitive nature of the electrode and electrolyte interface, direct

51 observation of surface species during electrochemical cycling
52 would help to clarify the involvement of oxygen. Previous
53 reports have made use of surface enhanced Raman spectros-
54 copy (SERS) to observe the oxygen-related reactions that occur
55 in a nonaqueous Li^+ electrolyte system on a Au electrode.¹³
56 Generally, any surface species formation is only observable
57 through the use of SERS-active substrates and not in an actual
58 working electrode due to the thin and small nature of the
59 surface formed. Here we demonstrate the application of SiO_2 -
60 coated Au nanoparticles that utilize SERS signal enhancement
61 on an LLNMO electrode to study the formation of surface
62 species during electrochemical cycling. While bare Au nano-
63 particles are not anticipated to participate or dramatically affect
64 the overall system, the insulating and inert SiO_2 coating insures
65 the isolation of the Au nanoparticle from the probed material
66 and avoids the special affinity associated with certain species
67 that may adsorb on to the nanoparticle. This SiO_2 coating also
68 serves to avoid the agglomeration of the nanoparticles that may
69 reduce signal enhancement.¹⁴ We show the ability of this
70 technique to directly observe Li_2O species formation during
71 charging and discuss the reactions that lead to its formation and
72 consumption. By combining previous observations with this
73 study's findings, we attempt to show the existence of the
74 different species formed at various stages of cycling and the

Received: October 2, 2013

75 formation of Li_2O , based on the participation of the anion and
76 thus link the different reactions that lead to changes within the
77 entire battery, including the cathode, anode, and electrolyte.

78 ■ EXPERIMENTAL SECTION

79 **Raw Materials.** Li_2O , Li_2O_2 , and MnCO_3 were purchased from
80 Sigma Aldrich; Li_2CO_3 , $\text{LiOH}\cdot\text{H}_2\text{O}$, $\text{Mn}(\text{SO}_4)\cdot\text{H}_2\text{O}$, and $\text{Ni}(\text{SO}_4)\cdot$
81 H_2O were purchased from Acros Organics; and Na_2CO_3 and NH_4OH
82 were purchased from J.T. Baker without modification or treatment.
83 Li_2O was stored in an Ar-filled glovebox with <1 ppm O_2 or H_2O
84 before analysis.

85 **Synthesis of the Lithium-Rich Cathode LLNMO.**
86 $\text{Li}_{1.2}\text{Ni}_{0.2}\text{Mn}_{0.6}\text{O}_2$ ($x = 0.2$) and $\text{LiNi}_{0.5}\text{Mn}_{0.5}\text{O}_2$ ($x = 0.5$) were
87 synthesized by a carbonate coprecipitation. Transition-metal sulfates
88 and Na_2CO_3 were separately dissolved in DI water. The mixed-metal
89 sulfate solution was slowly dripped into the Na_2CO_3 solution. After
90 stirring for 10 h the solution was vacuum-filtered, washed with DI
91 water, and dried overnight in a vacuum oven. The resulting
92 precipitates were mixed with Li_2CO_3 , fired at 900 °C for 12 h, and
93 then quenched to room temperature. The Li_2MnO_3 ($x = 0$) was
94 synthesized by grinding MnCO_3 and Li_2CO_3 in a Fritsch planetary ball
95 mill for 1 h at 150 rpm and then annealing at 400 °C for 32 h.¹⁵

96 **Characterization.** X-ray powder diffraction (XRD) was performed
97 on a Bruker D2 phaser diffractometer equipped with a $\text{Cu K}\alpha$
98 radiation source and a lynxeye detector. The surface morphologies and
99 particle sizes of the synthesized powders were examined using
100 scanning electron microscopy (JEOL, JSM 6500). Raman micro-
101 spectroscopy measurements were performed on a ProMaker system
102 mounted with one TE cooled CCD (1024 × 256 pixels) integrated by
103 Protrustech Corporation Limited. The system was equipped with a
104 50× long working distance lens (Olympus America inc.) operated with
105 an excitation wavelength of 532 nm, with ~1 mW laser power, unless
106 specified, to avoid degradation to the standards or electrodes.¹⁶ The
107 exposure time was 10 s with 10 accumulations. Calibration was done
108 using a silicon standard where the band is generally observed at 520
109 cm^{-1} . Raman analysis of Li_2O , Li_2O_2 , and $\text{LiOH}\cdot\text{H}_2\text{O}$ was undertaken
110 by placing the sample in a sealed holder with a 0.17 mm thick quartz
111 window prepared within in the Ar-filled glovebox.

112 **Electrode Fabrication.** The lithium-rich cathode was fabricated by
113 mixing the cathode powder, Super P carbon, and polyvinylidene
114 fluoride (PVdF) (weight ratio 80:10:10) to form a slurry using *N*-
115 methyl-2-pyrrolidone (NMP). The slurry was cast over an Al foil
116 which was then dried in a vacuum oven overnight. A graphite anode
117 was fabricated by mixing mesocarbon microbeads (MCMB-2528,
118 Osaka Gas), Super P conductive carbon, PVdF binder (weight ratio
119 90:7:3) to form a slurry using NMP. The slurry was cast over a Cu foil,
120 which was then dried in a vacuum oven overnight.

121 **Electrochemical Measurements.** A commercial electrolyte
122 comprising ethylene carbonate/diethyl carbonate (EC/DEC) 1:1
123 with added LiPF_6 (1 M) was used in a half-cell 2032 coin cell-type
124 battery with a Li foil counter electrode. Cyclic voltammetry (CV)
125 measurements were made using an Autolab potentiostat running at 0.1
126 mV/s from the open circuit potential to 5 V and then back to 2 V. The
127 charge and discharge measurements were run galvanostatically at 0.1 C
128 (C = 250 mAh/g) from 2.0–4.8 V.

129 **In situ SERS.** Au nanoparticles (NPs) 30–40 nm in diameter with a
130 SiO_2 coating (3–4 nm) were synthesized as in previous reports with
131 some modifications.¹⁷ Briefly, (3-aminopropyl) trimethoxysilane (1
132 mM) was added to the sol under vigorous magnetic stirring, followed
133 by the addition of a 0.54 wt % sodium silicate solution. The washed
134 and dried $\text{Au}@\text{SiO}_2$ NPs were transferred to an Ar-filled glovebox and
135 redispersed in diethyl carbonate (DEC). The NPs were dripped onto
136 the electrode surface and dried allowing the coin cell to be assembled.
137 A small hole was drilled in the top cap and stainless steel disk. A small
138 hole was also made in the lithium foil and separator in order to
139 observe the cathode's surface. After the coin cell was assembled, a 0.17
140 mm thick quartz window was applied to the top cap. All procedures
141 were undertaken in an Ar-filled glovebox with O_2 and H_2O levels

142 maintained at <1 ppm. CV was performed at 1 mV/s from 2 to 4.8 V
143 where the voltage was held before and during each acquisition.
144

145 **Raman Mapping.** The *in situ* SERS cathode electrodes were
146 extracted from the coin cell battery, washed with DEC, and placed
147 within a sealed holder. Spectral images were taken over a 100 × 100
148 μm area with 5 μm /point scan step with a 1 μm spatial resolution.
149

148 ■ RESULTS

149 **Raman, XRD, and SEM Characterization.** SEM measure-
150 ments with LLNMO $x = 0$, 0.2, and 0.5 can be seen in Figure
151 1a–c. Although Li_2MnO_3 was synthesized using a solid-state
152

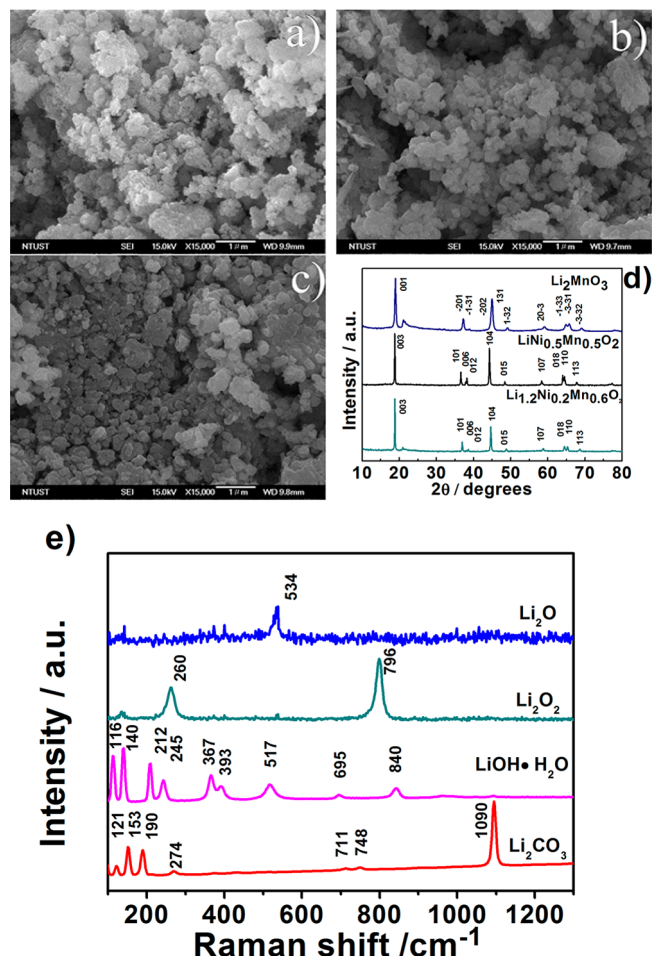


Figure 1. SEM images of: (a) Li_2MnO_3 , (b) $\text{LiNi}_{0.5}\text{Mn}_{0.5}\text{O}_2$, and (c) $\text{Li}_{1.2}\text{Ni}_{0.2}\text{Mn}_{0.6}\text{O}_2$; (d) shows XRD patterns for the three samples, while (e) shows the Raman spectra of the different standards.

153 method, all the samples have similar morphologies and particle
154 sizes ranging from 100 to 300 nm. XRD profiles are shown in
155 Figure 1d. The samples $\text{Li}_{1.2}\text{Ni}_{0.2}\text{Mn}_{0.6}\text{O}_2$ and $\text{LiNi}_{0.5}\text{Mn}_{0.5}\text{O}_2$
156 are indexed according to the parent hexagonal structure with
157 space group $\text{R}\bar{3}m$. The superlattice peak found at 20–25° for
158 $\text{Li}_{1.2}\text{Ni}_{0.2}\text{Mn}_{0.6}\text{O}_2$ corresponds to cation ordering within the
159 transition-metal plane between the Ni, Li, and Mn atoms.
160

161 Li_2MnO_3 is indexed according to the conventional
162 monoclinic cell with space group $\text{C}2/m$ where the peak around
163 20–25° is a superlattice peak from the ordering of the Li and
164 Mn atoms in the transition-metal layer. For Li_2MnO_3 , the
165 superlattice peak is broad, probably due to a large amount of
166 stacking faults in the material synthesized at low temperature.
167 Figure 1e shows the Raman spectra of several possible surface
168

166 species that will serve as reference compounds for comparison
 167 to the surface species formed on the electrodes during
 168 electrochemical cycling.^{13,18–20} Generally, Li_2CO_3 is the most
 169 commonly observed species on both the anode and cathode
 170 surfaces.^{19,21,22} $\text{LiOH}\cdot\text{H}_2\text{O}$ has been observed in some cases
 171 but is generally considered to be due to water contamination
 172 during electrode extraction during *ex situ* measurements.¹⁹ It
 173 should be noted that a band at 3567 cm^{-1} corresponding to the
 174 OH stretching mode is also observed for $\text{LiOH}\cdot\text{H}_2\text{O}$ (see
 175 Figure S1).²⁰ Li_2O_2 and Li_2O are generally found in $\text{Li}-\text{O}_2$
 176 battery systems, where *in situ* SERS utilizing a Au electrode was
 177 used to observe minute traces of the oxygen-related species that
 178 form on the surface of the electrode during electrochemical
 179 voltage steps.^{13,23–25}

180 **Electrochemical Measurements.** The CV profiles (first
 181 two cycles) of Li_2MnO_3 , $\text{LiNi}_{0.5}\text{Mn}_{0.5}\text{O}_2$, and $\text{Li}_{1.2}\text{Ni}_{0.2}\text{Mn}_{0.6}\text{O}_2$
 182 are shown in Figures 2a–c. The CV profile of Li_2MnO_3 is

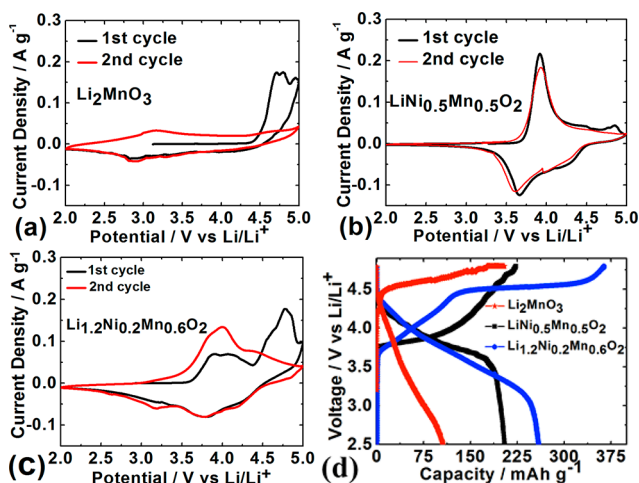


Figure 2. CV curves for the first 2 cycles of: (a) Li_2MnO_3 , (b) $\text{LiNi}_{0.5}\text{Mn}_{0.5}\text{O}_2$, and (c) $\text{Li}_{1.2}\text{Ni}_{0.2}\text{Mn}_{0.6}\text{O}_2$. (d) Charge and discharge curves for the first cycle for the three members.

183 shown in Figure 2a where the first cycle exhibits no oxidation
 184 peak until ~ 4.5 V after which the current increases steadily, due
 185 to simultaneous lithium extraction and oxygen activation. A
 186 reduction peak can be observed below 3.0 V for the first cycle
 187 corresponding to Mn^{3+} formation.²⁶ For the second cycle, the
 188 oxygen-activating reaction is not observed, indicating that this
 189 process is irreversible. An oxidation peak slightly above 3.0 V
 190 can be observed, together with a reduction peak below 3.0 V.
 191 These two peaks may correspond to the partial activity of the
 192 $\text{Mn}^{3+/4+}$ redox couple due to oxygen-activation reaction.²⁷ As
 193 shown in the CV profile of $\text{LiNi}_{0.5}\text{Mn}_{0.5}\text{O}_2$, see Figure 2b, the
 194 onset potential is ~ 3.7 V for the $\text{Ni}^{2+/4+}$ redox couple and ends
 195 at 4.4 V. Unlike Li_2MnO_3 , no major peak is observed for the
 196 higher voltage range, only a smaller peak at ~ 4.8 V which has
 197 been observed before.²⁸ This may be due to a small fraction of
 198 lithium-rich structure within the $\text{LiNi}_{0.5}\text{Mn}_{0.5}\text{O}_2$ that undergoes
 199 slight oxygen activation toward the end of charging. A
 200 reduction peak is observed with the lowest value centered at
 201 ~ 3.6 V which corresponds to the $\text{Ni}^{2+/4+}$ redox couple. No peak
 202 is observed below 3.0 V, indicating no Mn^{3+} formation after
 203 cycling. During the second cycle, only the $\text{Ni}^{2+/4+}$ redox pair
 204 undergoes oxidation and reduction, indicating that most of the
 205 charge compensation mechanism is due to the $\text{Ni}^{2+/4+}$ redox
 206 couple. The CV profile of $\text{Li}_{1.2}\text{Ni}_{0.2}\text{Mn}_{0.6}\text{O}_2$ is shown in Figure

2c where the onset, center, and ending potentials for the $\text{Ni}^{2+/4+}$ ²⁰⁷
 208 redox peak are observed at ~ 3.7 , ~ 4.0 , and ~ 4.5 V,²⁰⁹ respectively. The subsequent oxidation peak from 4.5 to 5.0 V²⁰⁹
 210 is similar to that representing simultaneous lithium extraction²¹⁰
 211 and oxygen activation, as seen in Figure 2a. During reduction,²¹¹
 212 the $\text{Ni}^{2+/4+}$ redox peak at ~ 3.6 V resembles $\text{LiNi}_{0.5}\text{Mn}_{0.5}\text{O}_2$,²¹²
 213 however below 3.6 V the current does not quickly decrease to zero²¹³
 214 but gradually drops in a similar manner to Li_2MnO_3 . For the second²¹⁴
 215 cycle, unlike $\text{LiNi}_{0.5}\text{Mn}_{0.5}\text{O}_2$, the Ni redox couple²¹⁵ does not entirely²¹⁶
 216 compensate for the large discharge capacity.²¹⁶ During oxidation,²¹⁷ the peak centered at 4.0 V shows an increase²¹⁷ in intensity that may be due to Mn or oxygen participation.²¹⁸ The²¹⁸
 219 higher voltage region does not show the oxygen-activating peak.²¹⁹
 220 For reduction, a smaller peak at ~ 3.2 V can be observed, similar²²⁰
 221 to Li_2MnO_3 , indicating the presence of Mn^{3+} .^{25,27} An obvious²²¹
 222 shoulder at around 4.3 V is thought to originate from the $\text{O}^{2-/}$ ²²²
 223 redox couple.^{27,29} Figure 2d shows the charge and discharge²²³
 224 curves for the three members of LLNMO. For Li_2MnO_3 , only²²⁴
 225 the plateau is observed in the high-voltage region, together with²²⁵
 226 a falling curve that gives a capacity of 100 mAh/g and an²²⁶
 227 irreversibly capacity (IC) of over 50% during discharge.²²⁷ $\text{LiNi}_{0.5}\text{Mn}_{0.5}\text{O}_2$ shows the solid solution line of the $\text{Ni}^{2+/4+}$ ²²⁸
 229 redox couple with a corresponding discharge curve showing²²⁹
 230 200 mAh/g with only 12% IC. $\text{Li}_{1.2}\text{Ni}_{0.2}\text{Mn}_{0.6}\text{O}_2$ shows a solid²³⁰
 231 solution line up to 120 mAh/g during charging, which is²³¹
 232 associated with the $\text{Ni}^{2+/4+}$ redox couple. A long plateau²³²
 233 corresponding to oxygen activation is followed and gives an²³³
 234 additional 250 mAh/g. Upon discharging, $\text{Li}_{1.2}\text{Ni}_{0.2}\text{Mn}_{0.6}\text{O}_2$ ²³⁴
 235 does not exhibit the plateau found during charging but a²³⁵
 236 sloping line showing 255 mAh/g with 32% IC.²³⁶

In Situ SERS. Figure 3a,b shows the *in situ* SERS spectra of²³⁷
 238 Li_2MnO_3 for charging and discharging, respectively. At the²³⁸
 239 open circuit potential (OCV), bands are found at 504 and 620²³⁹
 240 cm^{-1} . The band at 620 cm^{-1} corresponds to the A_{1g} mode of²⁴⁰
 241 Li_2MnO_3 ³⁰ and can be observed throughout charging. It moves²⁴¹
 242 to higher frequencies and returns to 620 cm^{-1} when discharged,²⁴²
 243 and the lower frequency band at 504 cm^{-1} has become²⁴³
 244 discernible indicating symmetry changes within the structure.³¹²⁴⁴
 245 The 504 cm^{-1} band also shows some distortion in the oxygen-²⁴⁵
 246 activation plateau region and also at 2.5 V, possibly due to the²⁴⁶
 247 dramatic structural rearrangements occurring in the plateau²⁴⁷
 248 region.³² When charging begins, a band at 1090 cm^{-1} emerges²⁴⁸
 249 corresponding to the CO_3 molecular unit.³³ This indicates the²⁴⁹
 250 formation of Li_2CO_3 that has also been observed in FTIR and²⁵⁰
 251 XPS when charged for other cathode materials^{21,22}. The Li_2O ²⁵¹
 252 band can be observed at 534 cm^{-1} when the voltage reaches²⁵²
 253 close to the oxygen-activating plateau (4.4 V) and reaches its²⁵³
 254 highest intensity at 4.52 V.²⁵⁴

A sharp band at 834 cm^{-1} can also be observed starting at 4.4 V,²⁵⁵
 256 which may correspond to the C–O stretching modes of an²⁵⁶
 257 ester, or ether, that forms due to electrolyte degradation.³⁴²⁵⁷
 258 Jiang et al.³⁵ have proposed that oxidation of the electrolyte²⁵⁸
 259 solvents forms organic species, such as aldehydes or ketones.²⁵⁹
 260 The band may also correspond to LiOH formed from Li_2O .³⁶²⁶⁰
 261 Once the end of charging is reached (4.8 V), the band of²⁶¹
 262 Li_2CO_3 gradually declines. This corresponds well with the²⁶²
 263 degradation of Li_2CO_3 at the charged state noted in previous²⁶³
 264 studies of LLNMO.^{11,12} Surprisingly, the Li_2O band also²⁶⁴
 265 gradually disappears at the end of charging. During discharging,²⁶⁵
 266 the 1090 cm^{-1} band of Li_2CO_3 reforms at 4.4 V and is present²⁶⁶
 267 after discharging to 2.0 V. *In situ* SERS spectra of²⁶⁷
 268 $\text{LiNi}_{0.5}\text{Mn}_{0.5}\text{O}_2$ for charging and discharging are shown in²⁶⁸
 269 Figure 3c,d, respectively. The E_g and A_{1g} bands are observed at²⁶⁹

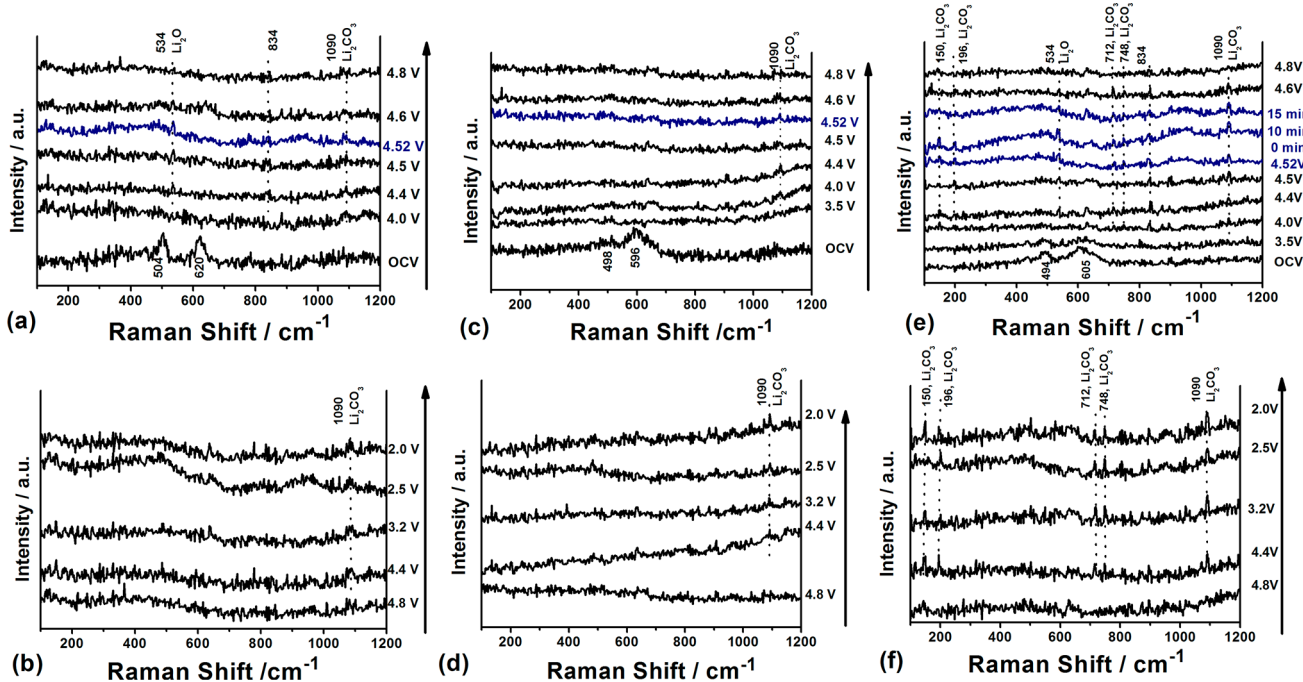


Figure 3. *In situ* SERS spectra of Li_2MnO_3 during (a) charging and (b) discharging; $\text{LiNi}_{0.5}\text{Mn}_{0.5}\text{O}_2$ during (c) charging and (d) discharging; and $\text{Li}_{1.2}\text{Ni}_{0.2}\text{Mn}_{0.6}\text{O}_2$ during (e) charging and (f) discharging. Arrows indicate voltage direction.

498 and 596 cm^{-1} , respectively. Similar to Li_2MnO_3 , these bands begin to lose intensity once the voltage begins to increase together with the emergence of the band at 1090 cm^{-1} corresponding to Li_2CO_3 . Throughout the first cycle, the band at 834 cm^{-1} was not observed, and no indication of Li_2O formation was apparent. Figure 3e,f shows the *in situ* SERS spectra of $\text{Li}_{1.2}\text{Ni}_{0.2}\text{Mn}_{0.6}\text{O}_2$ for charging and discharging, respectively, while the bands at 494 and 605 cm^{-1} correspond to the E_g mode and A_{1g} mode, respectively.³⁷ The A_{1g} mode can be seen to move to higher frequencies upon charging and shifts back to the lower frequency upon discharging. A distortion, similar to Li_2MnO_3 , to the E_g band region can also be seen during the plateau region, which may also be related to the structural rearrangement.³² When the electrode was discharged to 2.0 V, the A_{1g} and E_g modes can be observed, however the peaks are broader and the signal is much lower compared to the OCV state; this is similar to a previous *in situ* Raman spectroscopy study on the bulk changes within a similar material.³⁸ Unlike the current report, they did not observe surface formation where observation of Li_2CO_3 bands appear at 150, 196, 712, 748, and 1090 cm^{-1} . Similar to Li_2MnO_3 , the band at 834 is observed starting at 4.0 V. The Li_2O band can be observed when the voltage reaches close to the oxygen plateau (4.4 V) and continuously increases as the voltage increases to 4.52 V. Raman spectra were acquired while the voltage was held at 4.52 V for several minutes to observe if the Li_2O band would gradually decrease similarly to Li_2MnO_3 . The Li_2O band continues to increase (up to 10 min) and then subsequently decreases with increasing voltage. Possible reactions are proposed to consolidate the formation and consumption of Li_2O discussed later in this paper. Upon reaching 4.8 V, all bands dramatically decrease in intensity similar to Li_2MnO_3 . When discharging toward 2.0 V, the Li_2CO_3 bands appear as early as 4.4 V. This is in good agreement with previous reports that show the consumption of Li_2CO_3 at the top of the charge (4.8 V) and reformation when discharged.^{12,39} $\text{LiNi}_{0.5}\text{Mn}_{0.5}\text{O}_2$

does not exhibit the intense oxidation peak above ~ 4.5 V in its CV profile, which is observed with Li_2MnO_3 and $\text{L}_{1.2}\text{Ni}_{0.2}\text{Mn}_{0.6}\text{O}_2$, indicating that the formation of Li_2O is only observed with compositions exhibiting oxygen activation. The higher range from 3000 to 4000 cm^{-1} was taken for the initial, fully charged and discharged state (see Figure S2) in order to observe if there were any indications of water contamination before electrochemical measurements related to the formation of $\text{LiOH}\cdot\text{H}_2\text{O}$ or hydrolysis occurring: no OH band was observed.

The signals for several of the bands corresponding to the individual surface species, although discernible, are generally weak, similar to the SERS study of oxygen reaction in nonaqueous electrolyte on a Au electrode.¹³ To increase the signal from the different surface formations, *in situ* SERS for the $\text{Li}_{1.2}\text{Ni}_{0.2}\text{Mn}_{0.6}\text{O}_2$ and $\text{LiNi}_{0.5}\text{Mn}_{0.5}\text{O}_2$ compositions were repeated under the same conditions with only the laser power increased from 1 to 10 mW and then compared. In Figure 4, for both compositions, the bands corresponding to the surface formations have increased dramatically. The Li_2CO_3 bands are clearly seen beginning at 4.0 V as well as the C–O stretching band at 957 cm^{-1} upon charging. Li_2CO_3 bands decrease considerably at 4.8 V corresponding well with the 1 mW condition. In Figure 4a, the Li_2O band for $\text{Li}_{1.2}\text{Ni}_{0.2}\text{Mn}_{0.6}\text{O}_2$ can be clearly seen as the evolution follows the same trend as the 1 mW condition. In Figure 4b, no Li_2O band was observed for $\text{LiNi}_{0.5}\text{Mn}_{0.5}\text{O}_2$. Compared to the 1 mW condition, the band at 834 cm^{-1} was not observed for the $\text{Li}_{1.2}\text{Ni}_{0.2}\text{Mn}_{0.6}\text{O}_2$ composition during charging at 10 mW. This may be due to the increased probability of laser-induced degradation caused by the increased power, which has a much greater effect on organic species. Similar to the LLNMO taken at 1 mW, the voltage was held for several minutes to observe the evolution over time for the LLNMO at 10 mW laser power (see Figure S3). The Li_2O band increases upon reaching the

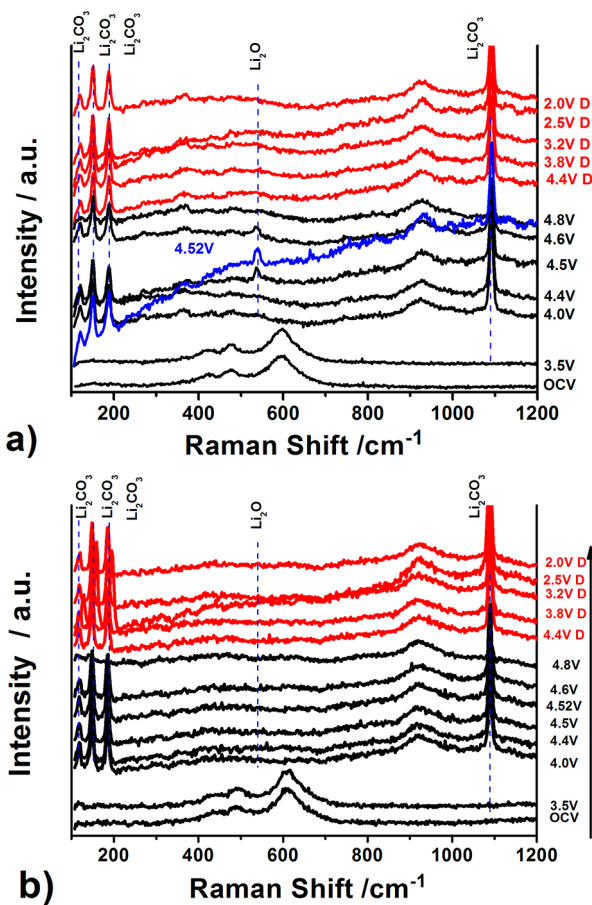


Figure 4. *In situ* SERS at 10 mW laser power for (a) $\text{Li}_{1.2}\text{Ni}_{0.2}\text{Mn}_{0.6}\text{O}_2$ and (b) $\text{LiNi}_{0.5}\text{Mn}_{0.5}\text{O}_2$.

341 plateau region and gradually decreases upon increasing the
342 voltage.

343 While the enhancements of Li_2O for 1 mW and 10 mW were
344 similar, Li_2CO_3 showed a more dramatic enhancement when
345 run under 10 mW laser power. Li_2CO_3 and Li_2O standards run
346 under both laser powers showed that this intensity increase is
347 related to the adjustment of the laser power (see Figure S4). It
348 should also be mentioned that without the use of a SERS probe
349 or substrate, the different surface formations would generally
350 not be observable under normal Raman conditions, especially
351 under *in situ* conditions, regardless of any adjustment to the
352 laser's power (see Figure S5). Furthermore, laser-induced
353 changes may occur if the laser power is increased.¹⁶

354 Observation of Li_2CO_3 surface coverage was done over a 100
355 \times 100 μm area of the electrode after discharging to 2.0 V by
356 mapping the 1090 cm^{-1} band. Figure 5a,b depicts
357 $\text{Li}_{1.2}\text{Ni}_{0.2}\text{Mn}_{0.6}\text{O}_2$ and $\text{LiNi}_{0.5}\text{Mn}_{0.5}\text{O}_2$, respectively. Examples
358 of the spectra for both of the electrodes can be found in the
359 Supporting Information (see Figure S6). Intensities below 1500
360 (black) counts are areas considered background. For
361 $\text{Li}_{1.2}\text{Ni}_{0.2}\text{Mn}_{0.6}\text{O}_2$, full coverage of Li_2CO_3 is observed within
362 the area, but several small areas show much higher intensities
363 where the population of Li_2CO_3 may be denser. The area
364 coverage is similar to observations under an optical microscope
365 done over a larger area where the formation of white particles
366 were observed.¹¹

367 In comparison, $\text{LiNi}_{0.5}\text{Mn}_{0.5}\text{O}_2$ shows large areas where the
368 signal drops below the background (black areas). The higher
369 coverage of Li_2CO_3 on the oxygen activating material agrees

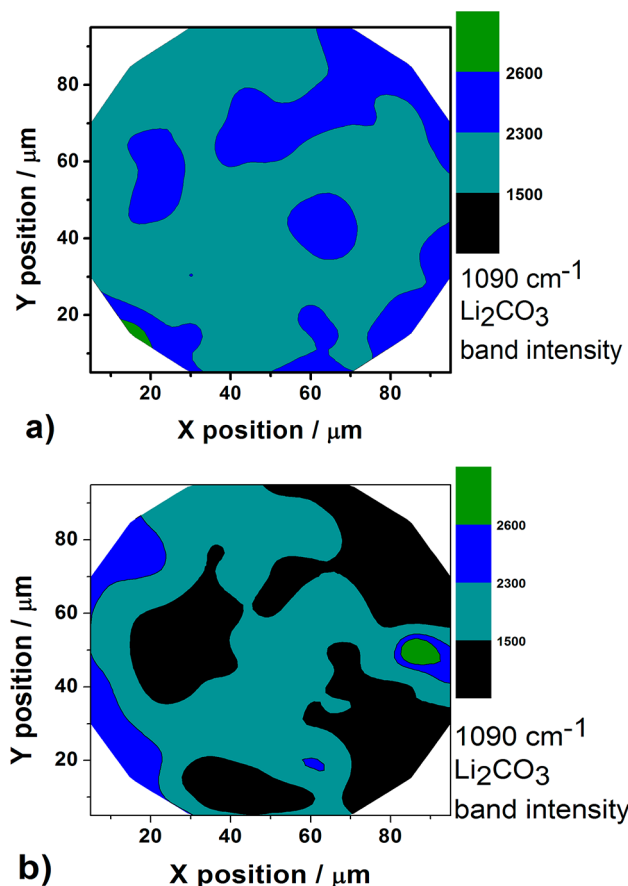


Figure 5. Raman mapping of (a) $\text{Li}_{1.2}\text{Ni}_{0.2}\text{Mn}_{0.6}\text{O}_2$ and (b) $\text{LiNi}_{0.5}\text{Mn}_{0.5}\text{O}_2$ after discharge to 2.0 V showing the 1090 cm^{-1} Li_2CO_3 band intensity.

well with previous studies showing high amounts of Li_2CO_3 after discharge.^{11,12}

■ DISCUSSION

For the Li-rich cathode material, the charge compensation mechanism generally starts by the compensation of the $\text{Ni}^{2+}/\text{Ni}^{4+}$ redox couple where ~ 0.4 Li^+ would be extracted. This would give a corresponding theoretical capacity of 126 mAh/g represented by reaction (1) in Table 1 where the potential t₁

Table 1. Different Reactions Occurring during Charging for $\text{Li}_{1.2}\text{Ni}_{0.2}\text{Mn}_{0.6}\text{O}_2$ up to 4.8 V

	reactions	E (V)
1	$\text{Li}_{1.2}\text{Ni}(\text{II})_{0.2}\text{Mn}(\text{IV})_{0.6}\text{O}(-\text{II})_2 \leftrightarrow \text{Li}_{1.2-0.2x}\text{Ni}(\text{II} + x)\text{O}_{0.2}\text{Mn}(\text{IV})_{0.6}\text{O}_2(-\text{II}) + 0.2\text{Li}^+ + 0.2e^-$ ($x \leq 2$) ($\text{Ni}^{2+}/\text{Ni}^{4+}$ redox couple)	≤ 4.4
2	$\text{Li}_{0.8}\text{Ni}(\text{IV})_{0.2}\text{Mn}(\text{IV})_{0.6}\text{O}(-\text{II})_2 \leftrightarrow \text{Li}_{0.8-2\delta}\text{Ni}(\text{IV})_{0.2}\text{Mn}(\text{IV})_{0.6}\text{O}(-\text{II} + \delta)_2 + 2\delta\text{Li}^+ + 2\delta e^-$ ($\text{O}^{2-}/\text{O}^{4-}$ redox couple)	$4.4 \leq E \leq 4.8$
3	$\text{Li}_{0.8}\text{Ni}(\text{IV})_{0.2}\text{Mn}(\text{IV})_{0.6}\text{O}(-\text{II})_2 \rightarrow \text{Li}_{0.8-2\delta}\text{Ni}(\text{IV})_{0.2}\text{Mn}(\text{IV})_{0.6}\text{O}(-\text{II})_{2-\delta} + \delta\text{Li}_2\text{O}$	$4.4 \leq E \leq 4.8$
4	$\text{Li}_{0.8-2\delta}\text{Ni}(\text{IV})_{0.2}\text{Mn}(\text{IV})_{0.6}\text{O}(-\text{II} + \delta)_2 + \text{solvents} \rightarrow \text{Li}_{0.8-2\delta}\text{Ni}(\text{IV})_{0.2}\text{Mn}(\text{IV})_{0.6}\text{O}(-\text{II} + \delta)_2 + \text{CO} \uparrow + \text{CO}_2 \uparrow + \text{other products} + \gamma \text{H}^+ + \gamma e^-$ (catalytic reaction)	$4.4 \leq E \leq 4.8$
5	$\text{Li}_{0.8-2\delta}\text{Ni}(\text{IV})_{0.2}\text{Mn}(\text{IV})_{0.6}\text{O}(-\text{II} + \delta)_2 \rightarrow \text{Li}_{0.8-2\delta}\text{Ni}(\text{IV})_{0.2}\text{Mn}(\text{IV})_{0.6}\text{O}(-\text{II})_{2-\delta} + \delta/2\text{O}_2 \uparrow$	$4.4 \leq E \leq 4.8$
6	$\text{Li}_2\text{O} + 2\text{H}^+ \rightarrow 2\text{Li}^+ + \text{H}_2\text{O}$	$4.4 \leq E \leq 4.8$
7	$\text{Li}_2\text{O} + \text{CO}_2 \rightarrow \text{Li}_2\text{CO}_3$	$4.4 \leq E \leq 4.8$

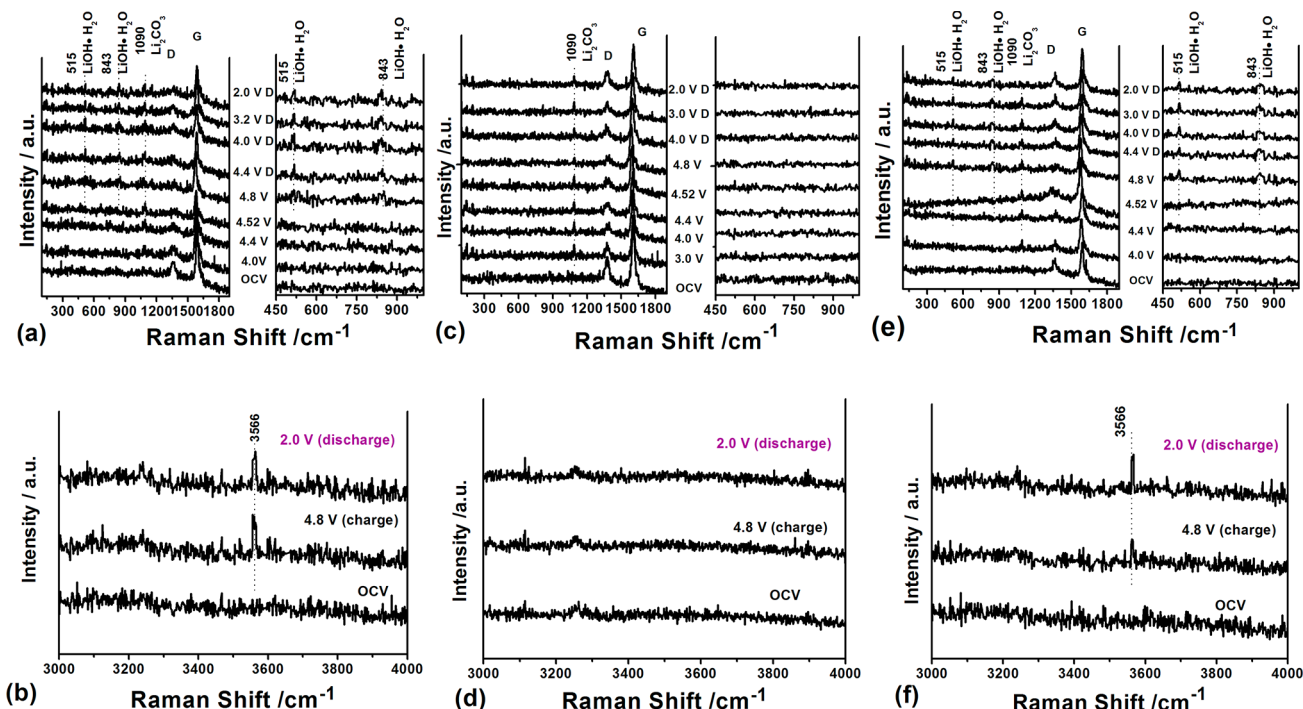


Figure 6. *In situ* SERS spectra of MCMB of the Li_2MnO_3 /MCMB battery for the (a) lower and (b) higher frequency range; $\text{LiNi}_{0.5}\text{Mn}_{0.5}\text{O}_2$ /MCMB battery for the (c) lower and (d) higher frequency range; and $\text{Li}_{1.2}\text{Ni}_{0.2}\text{Mn}_{0.6}\text{O}_2$ /MCMB battery for the (e) lower and (f) higher frequency range. D indicates discharge for the lower frequency.

378 range species when the specific reaction will likely occur. The
 379 possibility of Mn participation has been explored where Mn^{4+} is
 380 reduced after the first discharge (at least partially) to Mn^{3+}
 381 which can participate in subsequent cycles.^{11,29,40,41} Recently,
 382 several authors have focused on the participation of oxygen in
 383 the charging compensation beyond the $\text{Ni}^{2+/4+}$ redox.^{27,41–44}

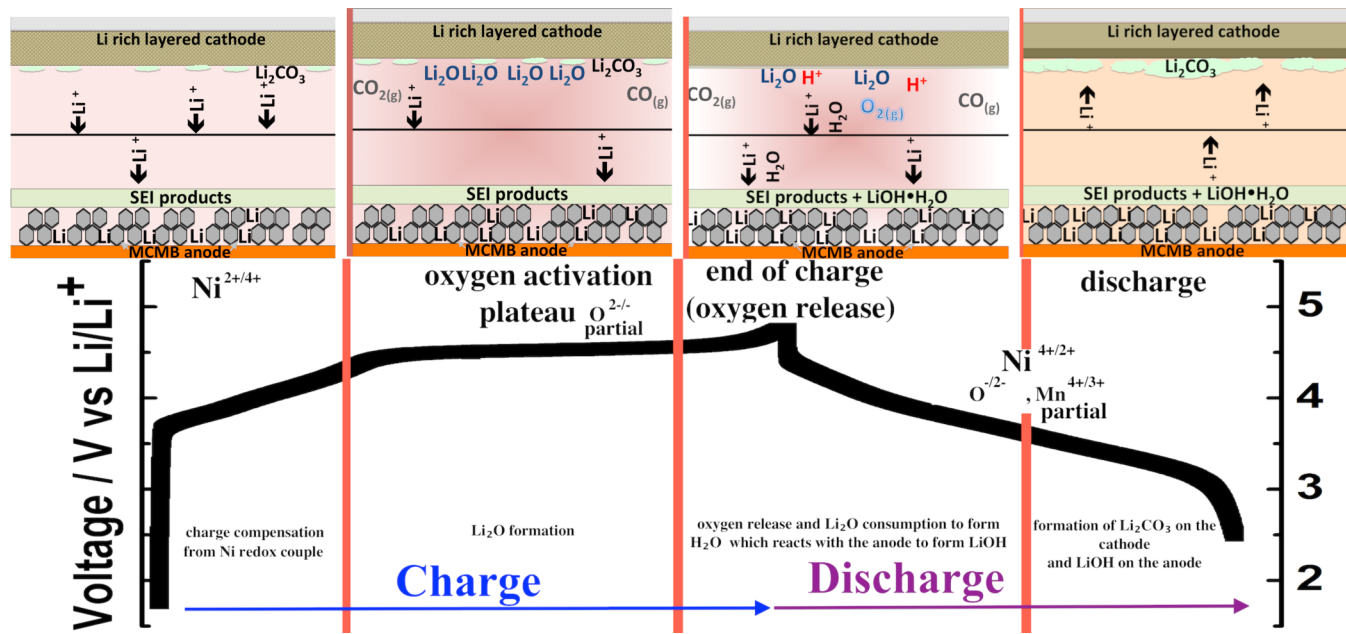
384 Fell et al.⁴⁴ have shown experimentally through Rietveld
 385 refinement of synchrotron XRD and EELS of the same
 386 material, the presence of oxygen vacancies and possible oxygen
 387 activation within the bulk structure. They explored the role of
 388 oxygen and suggested that the formation of oxygen vacancies
 389 associated with Mn reduction leads to the generation of Li_2O_2
 390 (via a superoxide) which reacts to form Li_2O .⁴¹

391 Koga et al.⁴³ similarly proposed the activation and
 392 participation of oxygen between two phases within
 393 $\text{Li}_{1.2}\text{Mn}_{0.54}\text{Co}_{0.13}\text{Ni}_{0.13}\text{O}_2$ in the charging mechanism through
 394 XRD analysis. Sathiya et al.²⁷ showed direct evidence of oxygen
 395 participation through XPS analysis at different charged states of
 396 $\text{Li}_2\text{Ru}_{0.5}\text{Mn}_{0.5}\text{O}_3$ where lattice oxygen was partially converted
 397 from O^{2-} to O^- after the oxygen plateau. Based on these
 398 previous studies of the anion redox participation, several
 399 possible reactions may take place and lead to the formation of
 400 Li_2O as well as other related products. When the oxidation of
 401 Ni^{2+} has reached an oxidation state of 4+, oxygen activation
 402 occurs following electrochemical reaction (2). Although this
 403 process is reversible, the activation of oxygen leaves the
 404 LLNMO highly reactive and highly unstable, i.e., similar to a
 405 catalyst or reactive species. After the occurrence of reaction (2),
 406 reactions (3–5) can occur with direct interaction of the
 407 LLNMO material where electrochemical reaction (3) forms
 408 Li_2O , which can be considered irreversible. It has been
 409 proposed that Li_2O may form from LiO_2 or Li_2O_2 , but neither
 410 LiO_2 nor Li_2O_2 were observed during the SERS measure-
 411 ments.⁴¹ Reaction (4) is the LLNMO oxygen activated material

reacting with the electrolyte solvents to form the electrolyte⁴¹²
 degradation products as well as a proton (H^+) and several gases⁴¹³
 such as CO_2 and CO through an irreversible catalytic reaction.⁴¹⁴
 Reaction (5), which is also irreversible, would be the third⁴¹⁵
 reaction that may also occur where O_2 gas would be released to⁴¹⁶
 stabilize the LLNMO material.⁴¹⁷

Regarding the evolution of the different gases, previous⁴¹⁸
 results have shown gas evolution during charging and⁴¹⁹
 specifically within the oxygen plateau region.^{12,35,45–47} Hong⁴²⁰
 et al.¹² showed, using differential electrochemical mass⁴²¹
 spectroscopy (DEMS), the formation of CO , CO_2 , and O_2 .⁴²² Interestingly,⁴²³ their results showed that gas formation occurred⁴²⁴
 from the middle toward the end of the plateau, reaching its⁴²⁵
 peak at the end of charge. Specifically, O_2 gas evolution did not⁴²⁶
 occur until the end of charge (4.8 V), while CO and CO_2 ⁴²⁷
 showed small accumulations in the middle of the plateau⁴²⁸
 (~ 4.55 V), increasing dramatically at the end of charge. Gas⁴²⁹
 evolution toward the end of charging rather than the beginning⁴³⁰
 of the plateau has also been observed by other workers.^{45–47}
 This suggests that reactions (4) and (5) are more significantly⁴³¹
 closer to the end of charging, while reaction (3) proceeds at the⁴³²
 beginning of the plateau region. However, it cannot be ruled⁴³³
 out that O_2 may have some degree of solubility into the⁴³⁴
 electrolyte, be consumed by the oxidation of lithium-organic⁴³⁵
 compounds, or take part in forming Li_2O .²⁴ Thus reaction (5)⁴³⁶
 may occur during the plateau where O_2 evolution only is⁴³⁷
 observed near the end-of-charge upon completing its reaction⁴³⁸
 or exceeding the solubility limit of the electrolyte. At the⁴³⁹
 beginning of discharge the generation of CO and CO_2 declines⁴⁴⁰
 rapidly, possibly reacting to form Li_2CO_3 and other products.⁴⁴¹ Interestingly,⁴⁴² CO and CO_2 evolution has been shown to⁴⁴³
 continue, at a reduced rate, after the first cycle, while O_2 ⁴⁴⁴
 evolution ceases after the first cycle.^{38,40} It is speculated that⁴⁴⁵
 reaction (4) may continue to occur after the first cycle causing⁴⁴⁶

Scheme 1. Proposed Surface Reaction Mechanism of $\text{Li}[\text{Ni}_x\text{Li}_{(1-2x)/3}\text{Mn}_{(2-x)/3}]\text{O}_2$ for Oxygen Activating Members during Charging and Discharging (top) and Charging/Discharging Curve Showing the Different Process (bottom)



446 continuous electrolyte decomposition leading to capacity fade,
 447 due to exhaustion of the electrolyte supply.³⁶

448 As mentioned above, during the oxygen-activating plateau,
 449 Li_2O is formed and then subsequently consumed toward the
 450 end of the plateau. The consumption of Li_2O would likely
 451 occur via reaction (6), i.e., with H^+ to form H_2O and/or (7)
 452 reacting with CO_2 to form Li_2CO_3 .

453 It should be noted that reactions (6) and (7) are not
 454 potential dependent but are chemical reactions dependent on
 455 the supply of Li_2O . It is possible that the generation of Li_2O
 456 from the electrochemical reaction and its consumption in
 457 reactions (6) and (7) take place simultaneously in the plateau
 458 region at a similar rate. When the end-of-plateau is reached and
 459 the potential further increases, the rate of Li_2O generation
 460 declines and is much lower than the rate of reaction (6) and
 461 (7). The presence of H_2O has previously been reported to lead
 462 to Mn dissolution and surface degradation and the dissolution
 463 of Mn.¹² In the presence of H_2O , the lithium salt may undergo
 464 reactions with LiPF_6 ¹² and other electrolyte components where
 465 it can form HF that is able to dissolve the material's surface.
 466 However, no indication of direct H_2O interaction on the
 467 cathode surface was observed during the first cycle *in situ*
 468 studies for the three LLNMO materials. The other possibility is
 469 the reaction of H_2O with the intercalated anode to form LiOH .
 470 Considering the high level of precipitation of Li_2CO_3 onto the
 471 cathode's surface at the discharged state, the interaction of Li_2O
 472 with H^+ and subsequent formation of LiOH may alter the
 473 electrolyte solution from acidic to more neutral. This would
 474 favor Li_2CO_3 precipitation by providing a favorable environ-
 475 ment for Li_2CO_3 to form on the surface of the cathode where
 476 the different gases, e.g., CO_2 , may dissolve into the electrolyte
 477 and react to form Li_2CO_3 .

478 In order to confirm changes within the electrolyte solution, *in*
 479 *situ* SERS was run to observe formation of $\text{LiOH}\cdot\text{H}_2\text{O}$ in a full
 480 cell configuration, which consisted of the LLNMO material
 481 with a small hole applied to the electrode and the $\text{Au}@\text{SiO}_2$ NP
 482 applied to the MCMB anode where the MCMB anode was the
 483 electrode probed. Figure 6a,b shows the Raman spectra

484 evolution of the MCMB anode in the $\text{Li}_2\text{MnO}_3/\text{MCMB}$ full 484
 485 cell during charging (insertion) and discharging (extraction), 485
 486 for the low- and high-frequency ranges, respectively. The 486
 487 evolution of the D (disorder-induced A_{1g} band) and G (C–C 487
 488 stretching mode, E_{2g}) band follows the evolution of Li 488
 489 insertion and extraction seen in other disordered graphite 489
 490 anodes⁴⁸ where the D band intensity slightly decreases ($I_{\text{G}}/I_{\text{D}}$ 490
 491 increases) and the G band moves from 1590 cm^{-1} toward the 491
 492 lower frequency during insertion before reaching the graphite 492
 493 dilute stage 1 and back to higher frequency during extraction.⁴⁸ 493

494 For the surface formation, at 4.0 V the peak at 1090 cm^{-1} 494
 495 corresponding to Li_2CO_3 formation can be observed and is 495
 496 present even after discharging to 2.0 V . Starting at the end of 496
 497 charging (4.8 V), two new bands appear at 515 and 843 cm^{-1} 497
 498 that correspond to $\text{LiOH}\cdot\text{H}_2\text{O}$ which remains after discharged 498
 499 to 2.0 V . The higher frequency range also shows the OH 499
 500 stretching band at 3566 cm^{-1} at the end of the charged (4.8 V) 500
 501 state and the discharged (2.0 V) state. Figure 6c,d shows the 501
 502 Raman spectra for the MCMB anode of the $\text{LiNi}_{0.5}\text{Mn}_{0.5}\text{O}_2/\text{MCMB}$ 502
 503 full cell (non- Li_2O forming material) for the lower and 503
 504 higher frequency ranges, respectively. The graphite bands 504
 505 during lithium insertion and extraction in the $\text{LiNi}_{0.5}\text{Mn}_{0.5}\text{O}_2/\text{MCMB}$ 505
 506 full cell show similar evolution to that of the $\text{Li}_2\text{MnO}_3/\text{MCMB}$ 506
 507 full cell. However, throughout the charging and 507
 508 discharging process, only the band corresponding to Li_2CO_3 508
 509 (1090 cm^{-1}) is present, and no indication of LiOH was found 509
 510 in the low or high frequency ranges. 510

511 Finally, to confirm the formation of LiOH occurring on the 511
 512 Li_2O forming materials series, the Raman measurements for the 512
 513 $\text{Li}_{1.2}\text{Ni}_{0.2}\text{Mn}_{0.6}\text{O}_2/\text{MCMB}$ full cell were performed, as shown in 513
 514 Figure 6e,f. The evolution of the graphite bands is similar to 514
 515 those previously described, except for a slight distortion of the 515
 516 spectra during charging at 4.52 V . Similar to the $\text{Li}_2\text{MnO}_3/\text{MCMB}$ 516
 517 full cell, LiOH bands at low and high frequencies can 517
 518 be seen at the end of charge that remain after discharging to 2.0 V . 518
 519 This confirms the formation of LiOH , by the interaction of 519
 520 H_2O formed from Li_2O . 520

To further confirm the changes to the electrolyte system, favoring precipitation of the surface deposits, the electrolyte pH was investigated using $\text{Li}_{1.2}\text{Ni}_{0.2}\text{Mn}_{0.6}\text{O}_2$ batteries run in an Ar-filled glovebox and stopped at different potentials. The batteries were then opened, and the pH of the electrolyte was quickly measured by litmus paper (see Figure S9).

When charged before reaching the plateau (4.4 V) the solution changes to a more acidic environment than the solution at OCV and maintains this environment when discharged to 2.5 V. When charged to 4.8 V (after the plateau has finished) and discharged to 2.5 V, the solution changes from an acidic environment before and during the plateau to a more neutral environment after discharged. This confirms that the presence of Li_2O evolution will change the electrolyte solution environment from acidic to more neutral, while in the absence of it there is not such a dramatic change. Lee et al.⁴⁹ showed that LiCoO_2 and LiCoPO_4 under oxygen evolution reaction conditions, at varying pH values, the cathode's surface will either be amorphous (pH = 13) or spinel (pH = 7). Previous reports^{7,29} have shown the conversion of a layered to a spinel surface when continuously cycled, and several workers have shown HRTEM images of the growth of an amorphous layer.^{12,50} This correlates well with the changes of the surface of the material with the electrolyte condition.

Scheme 1 illustrates the proposed surface reaction mechanism for LLNMO that occurs during charging and discharging for oxygen activating members, based on the results of the previous studies mentioned in the article and the surface reactions observed for the cathode and anode sides during the *in situ* SERS studies. Before the plateau the formation of the SEI on the anode side occurs with a limited formation of Li_2CO_3 on the cathode side from the interaction with the electrolyte where the charge compensation follows the $\text{Ni}^{2+}/\text{Ni}^{4+}$ redox couple. During the plateau, activation of oxygen occurs as well as Li_2O formation. Electrolyte degradation may also occur, forming gases such as CO and CO_2 . Toward the end of the plateau, the unstable and catalyst-like LLNMO material causes the release of O_2 gas as well as readily reacting with the electrolyte to form CO, CO_2 , and protons (H^+) via a catalytic reaction. Li_2O will react with the proton (H^+) to form Li^+ and H_2O which solvates and migrates to the anode side forming $\text{LiOH}\cdot\text{H}_2\text{O}$ at the end of charging. The discharge compensation mechanism is thought to be a combination of the $\text{Ni}^{2+}/\text{Ni}^{4+}$ redox couple, oxygen anion redox couple, and the partial participation of $\text{Mn}^{3+}/\text{Mn}^{4+}$ that continually grows with increasing cycles. It should be noted, although changes have been observed, the role of Mn in the charging compensation mechanism is still not clear but may be related to bulk stabilization. Toward the end of the discharging process, the reaction of H^+ and formation of LiOH leads to the solution changes from an acidic to a more neutral environment leading to highly cathodic Li_2CO_3 precipitation that leads to a diminished performance.

In summary, by using *in situ* SERS to observe surface phenomena for both the anode and the cathode, we have provided direct evidence of Li_2O formation on lithium-rich cathode materials and the formation of $\text{LiOH}\cdot\text{H}_2\text{O}$ on the anode. The consequences of this formation and a comprehensive mechanism were discussed considering oxygen anion redox charge compensation. Upon reaching the plateau at ~ 4.5 V where oxygen is activated, the formation of Li_2O and its subsequent reactions lead to the hydrolysis of the electrolyte, and changes within the solution lead to the formation of Li_2CO_3 and other related products when discharged. Our

results suggest that consideration of both the cathode and anode is crucial to elucidating the nature of the reactions occurring within the entire battery system to improve its performance. Furthermore focusing on not only surface coatings to improve the stability but also on the electrolyte should provide a route to improve the performance of these materials.

ASSOCIATED CONTENT

Supporting Information

Raman spectra for $\text{Li}_{1.2}\text{Ni}_{0.2}\text{Mn}_{0.6}\text{O}_2$ cathode and MCMB anode, *in situ* SERS spectra and normal Raman comparison, SERS spectra running at constant current charging protocol, Raman spectra for mapping, and images of pH measurements. This material is available free of charge via the Internet at <http://pubs.acs.org>.

AUTHOR INFORMATION

Corresponding Author

bjh@mail.ntust.edu.tw

Notes

The authors declare no competing financial interest.

ACKNOWLEDGMENTS

Financial support from the National Science Council (NSC) grant nos. (101-3113-E-011-002, 101-2923-E-011-001-MY3, 100-2221-E-011-105-MY3), the Ministry of Economic Affairs (MOEA) (101-EC-17-A-08-S1-183), and the Top University Projects of Ministry of Education (MOE) (100H451401) as well as the facilities support from the National Taiwan University of Science and Technology (NTUST) are acknowledged. Damien S. Clark for his insightful discussions and suggestions.

REFERENCES

- (1) Lu, Z.; MacNeil, D. D.; Dahn, J. R. *Electrochem. Solid-State Lett.* **2001**, *4*, A191.
- (2) Johnson, C. S.; Kim, J. S.; Lefief, C.; Li, N.; Vaughey, J. T.; Thackeray, M. M. *Electrochem. Commun.* **2004**, *6*, 1085.
- (3) Thackeray, M. M.; Johnson, C. S.; Vaughey, J. T. *J. Mater. Chem.* **2005**, *15*, 2257.
- (4) Hwang, B. J.; Wang, C. J.; Chen, C. H.; Tsai, Y. W.; Venkateswarlu, M. *J. Power Sources* **2005**, *146*, 658.
- (5) Lu, Z.; Dahn, J. R. *J. Electrochem. Soc.* **2002**, *149*, A815.
- (6) Jarvis, K. A.; Deng, Z.; Allard, L. F.; Manthiram, A.; Ferreira, P. J. *Chem. Mater.* **2011**, *23*, 3614.
- (7) Gu, M.; Belharouak, I.; Zheng, J.; Wu, H.; Xiao, J.; Genc, A.; Amine, K.; Thevuthasan, S.; Baer, D. R.; Zhang, J.-G.; Browning, N. D.; Liu, J.; Wang, C. *ACS Nano* **2012**, *7*, 760.
- (8) Hu, M.; Pang, X.; Zhou, Z. *J. Power Sources* **2013**, *237*, 229.
- (9) Ohzuku, T.; Nagayama, M.; Tsuji, K.; Ariyoshi, K. *J. Mater. Chem.* **2011**, *21*, 10179.
- (10) Thackeray, M. M.; Kang, S.-H.; Johnson, C. S.; Vaughey, J. T.; Benedek, R.; Hackney, S. A. *J. Mater. Chem.* **2007**, *17*, 3112.
- (11) Yabuuchi, N.; Yoshii, K.; Myung, S.-T.; Nakai, I.; Komaba, S. *J. Am. Chem. Soc.* **2011**, *133*, 4404.
- (12) Hong, J.; Lim, H.-D.; Lee, M.; Kim, S.-W.; Kim, H.; Oh, S.-T.; Chung, G.-C.; Kang, K. *Chem. Mater.* **2012**, *24*, 2692.
- (13) Peng, Z.; Freunberger, S. A.; Hardwick, L. J.; Chen, Y.; Giordani, V.; Barde, F.; Novak, P.; Graham, D.; Tarascon, J. M.; Bruce, P. G. *Angew. Chem., Int. Ed. Engl.* **2011**, *50*, 6351.
- (14) Li, J.-F.; Li, S.-B.; Anema, J. R.; Yang, Z.-L.; Huang, Y.-F.; Ding, Y.; Wu, Y.-F.; Zhou, X.-S.; Wu, D.-Y.; Ren, B.; Wang, Z.-L.; Tian, Z.-Q. *Appl. Spectrosc.* **2011**, *65*, 620.
- (15) Yu, D. Y. W.; Yanagida, K. *J. Electrochem. Soc.* **2011**, *158*, A1015.

645 (16) Burba, C. M.; Palmer, J. M.; Holinsworth, B. S. *J. Raman*
646 *Spectrosc.* **2009**, *40*, 225.

647 (17) Li, J. F.; Huang, Y. F.; Ding, Y.; Yang, Z. L.; Li, S. B.; Zhou, X.
648 S.; Fan, F. R.; Zhang, W.; Zhou, Z. Y.; Wu, D. Y.; Ren, B.; Wang, Z. L.;
649 Tian, Z. Q. *Nature* **2010**, *464*, 392.

650 (18) Thapa, A. K.; Saimen, K.; Ishihara, T. *Electrochem. Solid-State*
651 *Lett.* **2010**, *13*, A165.

652 (19) Verma, P.; Maire, P.; Novák, P. *Electrochim. Acta* **2010**, *55*, 6332.

653 (20) Li, G.; Li, H.; Mo, Y.; Chen, L.; Huang, X. *J. Power Sources* **2002**,
654 *104*, 190.

655 (21) Dedryvère, R.; Martinez, H.; Leroy, S.; Lemordant, D.;
656 Bonhomme, F.; Biensan, P.; Gonbeau, D. *J. Power Sources* **2007**,
657 *174*, 462.

658 (22) Matsui, M.; Dokko, K.; Kanamura, K. *J. Power Sources* **2008**,
659 *177*, 184.

660 (23) Peng, Z.; Freunberger, S. A.; Chen, Y.; Bruce, P. G. *Science*
661 **2012**, *337*, 563.

662 (24) Schroder, K. W.; Celio, H.; Webb, L. J.; Stevenson, K. J. *J. Phys.*
663 *Chem. C* **2012**, *116*, 19737.

664 (25) Freunberger, S. A.; Chen, Y.; Peng, Z.; Griffin, J. M.; Hardwick,
665 L. J.; Barde, F.; Novak, P.; Bruce, P. G. *J. Am. Chem. Soc.* **2011**, *133*,
666 8040.

667 (26) Paulsen, J. M.; Thomas, C. L.; Dahn, J. R. *J. Electrochem. Soc.*
668 **2000**, *147*, 861.

669 (27) Sathiya, M.; Ramesha, K.; Rousse, G.; Foix, D.; Gonbeau, D.;
670 Prakash, A. S.; Doublet, M. L.; Hemalatha, K.; Tarascon, J. M. *Chem.*
671 *Mater.* **2013**, *25*, 1121.

672 (28) Gopukumar, S.; Chung, K. Y.; Kim, K. B. *Electrochim. Acta* **2004**,
673 *49*, 803.

674 (29) Hy, S.; Su, W.-N.; Chen, J.-M.; Hwang, B.-J. *J. Phys. Chem. C*
675 **2012**, *116*, 25242.

676 (30) Julien, C. M.; Massot, M. *Mater. Sci. Eng., B* **2003**, *100*, 69.

677 (31) Amalraj, S. F.; Sharon, D.; Taliander, M.; Julien, C. M.; Burlaka,
678 L.; Lavi, R.; Zhecheva, E.; Markovsky, B.; Zinograd, E.; Kovacheva, D.;
679 Stoyanova, R.; Aurbach, D. *Electrochim. Acta* **2013**, *97*, 259.

680 (32) Tran, N.; Croguennec, L.; Ménétrier, M.; Weill, F.; Biensan, P.;
681 Jordy, C.; Delmas, C. *Chem. Mater.* **2008**, *20*, 4815.

682 (33) Okazaki, S.; Ohtori, N.; Okada, I. *J. Chem. Phys.* **1989**, *91*, 5587.

683 (34) Larkin, P. *Infrared and Raman Spectroscopy: principles and*
684 *spectral interpretation*; Elsevier, Inc.: Waltham, MA, 2011.

685 (35) Jiang, M.; Key, B.; Meng, Y. S.; Grey, C. P. *Chem. Mater.* **2009**,
686 *21*, 2733.

687 (36) Black, R.; Oh, S. H.; Lee, J.-H.; Yim, T.; Adams, B.; Nazar, L. F.
688 *J. Am. Chem. Soc.* **2012**, *134*, 2902.

689 (37) Hong, J.; Seo, D.-H.; Kim, S.-W.; Gwon, H.; Oh, S.-T.; Kang, K.
690 *J. Mater. Chem.* **2010**, *20*, 10179.

691 (38) Singh, G.; West, W. C.; Soler, J.; Katiyar, R. S. *J. Power Sources*
692 **2012**, *218*, 34.

693 (39) Yabuuchi, N.; Yoshii, K.; Myung, S. T.; Nakai, I.; Komaba, S. *J.*
694 *Am. Chem. Soc.* **2011**, *133*, 4404.

695 (40) Ito, A.; Sato, Y.; Sanada, T.; Hatano, M.; Horie, H.; Ohsawa, Y.
696 *J. Power Sources* **2011**, *196*, 6828.

697 (41) Carroll, K. J.; Qian, D.; Fell, C.; Calvin, S.; Veith, G. M.; Chi,
698 M.; Baggetto, L.; Meng, Y. S. *Phys. Chem. Chem. Phys.* **2013**, *15*, 11128.

699 (42) Oishi, M.; Fujimoto, T.; Takanashi, Y.; Oriksa, Y.; Kawamura,
700 A.; Ina, T.; Yamashige, H.; Takamatsu, D.; Sato, K.; Murayama, H.;
701 Tanida, H.; Arai, H.; Ishii, H.; Yogi, C.; Watanabe, I.; Ohta, T.;
702 Mineshige, A.; Uchimoto, Y.; Ogumi, Z. *J. Power Sources* **2013**, *222*, 45.

703 (43) Koga, H.; Croguennec, L.; Ménétrier, M.; Mannessiez, P.; Weill,
704 F.; Delmas, C. *J. Power Sources* **2013**, *236*, 250.

705 (44) Fell, C. R.; Qian, D.; Carroll, K. J.; Chi, M.; Jones, J. L.; Meng,
706 Y. S. *Chem. Mater.* **2013**, *25*, 1621.

707 (45) Lanz, P.; Sommer, H.; Schulz-Dobrick, M.; Novák, P.
708 *Electrochim. Acta* **2013**, *93*, 114.

709 (46) La Mantia, F.; Rosciano, F.; Tran, N.; Novák, P. *J. Appl.*
710 *Electrochem.* **2008**, *38*, 893.

711 (47) Armstrong, A. R.; Holzapfel, M.; Novák, P.; Johnson, C. S.;
712 Kang, S.-H.; Thackeray, M. M.; Bruce, P. G. *J. Am. Chem. Soc.* **2006**,
713 *128*, 8694.

(48) Hardwick, L.; Buqa, H.; Novák, P. *Solid State Ionics* **2006**, *177*, 714
2801. 715

(49) Lee, S. W.; Carlton, C.; Risch, M.; Surendranath, Y.; Chen, S.; 716
Furutsuki, S.; Yamada, A.; Nocera, D. G.; Shao-Horn, Y. *J. Am. Chem. 717*
Soc. **2012**, *134*, 16959. 718

(50) Xu, B.; Fell, C. R.; Chi, M.; Meng, Y. S. *Energy Environ. Sci.* **2011**, *4*, 2223. 719
720